Sustained Notch2 signaling in osteoblasts, but not in osteoclasts, is linked to osteopenia in a mouse model of Hajdu-Cheney syndrome

Stefano Zanotti[‡§¶], Jungeun Yu[‡¶], Archana Sanjay[‡¶], Lauren Schilling[¶], Chris Schoenherr[‖], Aris N. Economides[‖], and ⓘ Ernesto Canalis[‡§¶1]

From the Departments of ‡Orthopaedic Surgery and §Medicine, and the ¶UConn Musculoskeletal Institute, UConn Health, Farmington, Connecticut 06030 and ‖Regeneron Pharmaceuticals, Tarrytown, New York 10591

Edited by Jeffrey E. Pessin

Individuals with Hajdu-Cheney syndrome (HCS) present with osteoporosis, and HCS is associated with *NOTCH2* mutations causing deletions of the proline-, glutamic acid-, serine-, and threonine-rich (PEST) domain that are predicted to enhance NOTCH2 stability and cause gain-of-function. Previously, we demonstrated that mice harboring *Notch2* mutations analogous to those in HCS (*Notch2HCS*) are severely osteopenic because of enhanced bone resorption. We attributed this phenotype to osteoclastic sensitization to the receptor activator of nuclear factor-κB ligand and increased osteoblastic tumor necrosis factor superfamily member 11 (*Tnfsf11*) expression. Here, to determine the individual contributions of osteoclasts and osteoblasts to HCS osteopenia, we created a conditional-by-inversion (*Notch2^COIN*) model in which Cre recombination generates a *Notch2^ΔPEST* allele expressing a Notch2 mutant lacking the PEST domain. Germ line *Notch2^COIN* inversion phenocopied the *Notch2HCS* mutant, validating the model. To activate Notch2 in osteoclasts or osteoblasts, *Notch2^COIN* mice were bred with mice expressing Cre from the *Lyz2* or the *BGLAP* promoter, respectively. These crosses created experimental mice harboring a *Notch2^ΔPEST* allele in Cre-expressing cells and control littermates expressing a wild-type *Notch2* transcript. *Notch2^COIN* inversion in *Lyz2*-expressing cells had no skeletal consequences and did not affect the capacity of bone marrow macrophages to form osteoclasts *in vitro*. In contrast, *Notch2^COIN* inversion in osteoblasts led to generalized osteopenia associated with enhanced bone resorption in the cancellous bone compartment and with suppressed endocortical mineral apposition rate. Accordingly, *Notch2* activation in osteoblast-enriched cultures from *Notch2^COIN* mice induced *Tnfsf11* expression. In conclusion, introduction of the HCS mutation in osteoblasts, but not in osteoclasts, causes osteopenia.

Notch signaling plays a fundamental role in cell fate determination (1). Interactions of the four Notch receptors with cognate ligands of the Jagged and Delta-like families lead to the proteolytic cleavage of the receptor and the release of the Notch intracellular domain (NICD)[2] from the cellular membrane (2). Subsequently, the NICD translocates to the nucleus and forms a complex with recombination signal-binding protein for the immunoglobulin κJ region (Rbpjκ), mastermind-like (Maml), and additional DNA-associated proteins to elicit a transcriptional response (3). These events result in the induction of Notch target genes, such as *Hes1*, *Hey1*, *Hey2*, and *HeyL* (4). Although this signaling mechanism is shared by the Notch paralogs, each receptor has distinct functions (5). The reason appears to be related to the differential cellular pattern of expression of the receptors, structural differences between the paralogs, and interactions of the individual NICDs with Rbpjκ (6–8).

Bone remodeling is the process whereby the coordinated activities of osteoclasts and osteoblasts preserve skeletal integrity (9). Osteoclasts are multinucleated bone-resorbing cells formed by the fusion of mononuclear myeloid precursors in the presence of receptor activator of nuclear factor κB ligand (Rankl), a protein encoded by *Tnfsf11*, and macrophage colony-stimulating factor (M-CSF) (10). Osteoblasts are bone-forming cells of mesenchymal origin that regulate bone resorption by secreting Rankl and its decoy receptor, osteoprotegerin (9, 11). Notch1 and Notch2 exhibit distinct functions in skeletal cells, and tight regulation of their activity is essential to maintain bone remodeling (12). Notch1 inhibits osteoclastogenesis and osteoblastogenesis, whereas Notch2 inhibits osteoblast differentiation/function but stimulates osteoclastogenesis (13–19).

Hajdu-Cheney syndrome (HCS) is a rare and devastating disease with multiple systemic manifestations, including osteopo-

[2] The abbreviations used are: NICD, Notch intracellular domain; Ad, adenovirus; α-MEM, α-minimum essential medium; ATCC, American Type Culture Collection; BMM, bone marrow-derived macrophage; CMV, cytomegalovirus; eGFP, enhanced green fluorescent protein; FLP, flippase; FRT, FLP recognition target; HCS, Hajdu-Cheney syndrome; kb, kilobase; *L66*, *lox66*; *L71*, *lox71*; *L72*, *lox72*; IDT, Integrated DNA Technologies; M-CSF, macrophage-colony-stimulating factor; μCT, microcomputed tomography; PEST, proline- (P), glutamic acid- (E), serine- (S), and (T) threonine-rich; qRT-PCR, quantitative reverse transcription-PCR; rβglpA, β-globin polyadenylation signal; Rankl, receptor activator of nuclear factor κB ligand; Rbpjκ, recombination signal binding protein for immunoglobulin κJ region; Trap, tartrate-resistant acid phosphatase; SMI, structure model index.
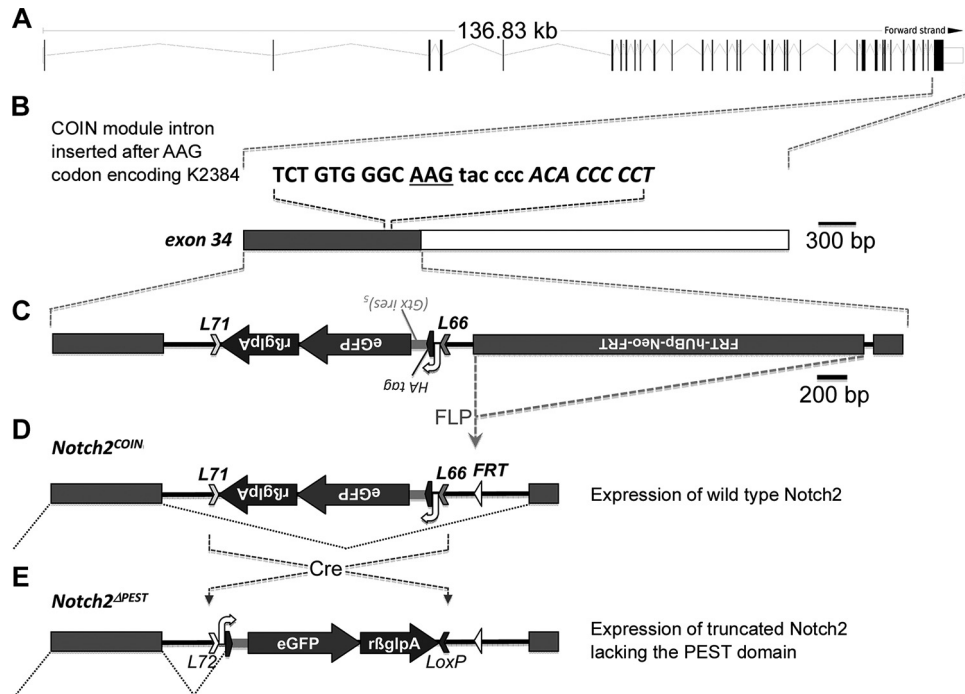
Figure 1. Engineering of the *Notch2^COIN* allele. *A,* genomic structure and size of the *Notch2* locus with the position of the 34 exons indicated by *vertical black bars* for coding sequences or *white boxes* for untranslated regions (UTR). *B,* position of the AAG codon (*underlined*) for lysine 2384 in exon 34. The sequence of the insertion site of the *COIN* module is in *lowercase*, and *gray* and *white boxes* indicate the coding sequence and the 3'-UTR (*rβglpA*), respectively. *C,* structure of exon 34 and of the targeting construct correctly integrated. From 5' to 3': *lox71* (*L71*), rabbit β-globin polyadenylation signal, eGFP-coding sequence, internal ribosome entry site (*Gtx ires*)₅, human influenza hemagglutinin (HA) tag coding sequence, 3'-splice region from the second intron of the rabbit β-globin gene (*white curved arrow*), and *lox66* (*L66*) that constitute the *COIN* module and a flippase (FLP) recognition site (FRT)-flanked *neo* cassette downstream of the human *UBp* promoter (*FRT-hUBp-neo-FRT*). Removal of the *neo* cassette by FLP recombination is indicated (*gray dotted lines*). *D,* representation of the silent COIN module in the antisense orientation and of the splicing event (*black dotted lines*) that excises the *COIN* module from the nascent transcript, allowing expression of a wild-type Notch2 mRNA and protein. *E,* generation of the *Notch2^ΔPEST* allele by Cre recombinase-mediated permanent inversion of the *COIN* module, and illustration of the splicing event (*black dotted lines*) that occurs during the maturation of the *Notch2^ΔPEST* transcript. The latter is translated into a Notch2 mutant lacking the PEST domain. The position of the silent *lox72* (*L72*) sequence and of the wild-type *loxP* site created by Cre recombination of *L71* and *L66* is indicated. Images are scaled either in kilobase (*kb*) or bp.

rosis, short stature, craniofacial deformities, and acroosteolysis (20, 21). The condition is associated with mutations in exon 34 of *NOTCH2* that create a premature stop codon immediately upstream of the sequences coding for the proline- (P), glutamic acid- (E), serine- (S), and (T) threonine-rich (PEST) domain (22–26). The latter is required for the proteasomal degradation of NOTCH2, so that the mutations are predicted to lead to the translation of a stable NOTCH2 protein with sustained activity. Recently, we established a murine model of HCS by introducing the mutation found in a subject with severe osteoporosis into the mouse genome. The mutant, termed *Notch2HCS*, expresses a Notch2 protein of 2318 amino acids that lacks the PEST domain. Heterozygous *Notch2HCS* mice exhibit *Notch2* gain-of-function and generalized osteopenia secondary to enhanced bone resorption, which was ascribed to the sensitization of osteoclast precursors to Rankl and increased *Tnfsf11* expression in osteoblasts (27). However, the individual contribution of cells of the osteoclast and osteoblast lineages to the osteopenic phenotype of *Notch2HCS* mice remains to be determined.

In this study, a conditional by inversion (COIN) approach was utilized to create a conditional mouse model of HCS (*Notch2^COIN*) (28, 29). This system was designed to introduce a premature STOP codon in exon 34 of *Notch2* following Cre-mediated recombination leading to the translation of a truncated Notch2 protein, thus mimicking the genetic defect

associated with HCS. To study the consequences of the Notch2 truncation in specific skeletal cell lineages, *Notch2* conditional mice were crossed with appropriate Cre drivers to introduce the mutation in cells of the osteoclast (*Lyz2^Cre*) or osteoblast (*BGLAP-Cre*) lineages. Mutant and control mice were examined for skeletal phenotypic changes by microcomputed tomography (μCT) and bone histomorphometry, and the potential mechanisms of Notch2 action were explored.

Results

Generation of a conditional HCS mouse model

To induce the HCS mutation in selected cell populations, *Notch2^COIN* mice were created by inserting an artificial *COIN* intron into exon 34 of the murine *Notch2* locus (Fig. 1*A*). As a result, exon 34 was split into two exons at a position corresponding to lysine 2384, which is upstream of the PEST domain and downstream of the domains required for the transcriptional activation of Notch2 (NCBI protein database NP035058; Fig. 1*B*). The *COIN* module is composed of a gene trap-like *lox66_HA-egfp-polyA_lox71* cassette encoding for a hemagglutinin (HA)-internal ribosome entry site and enhanced green fluorescent protein (eGFP) and placed in the antisense strand. The cassette is preceded by a 3'-splice region derived from the second intron of rabbit *HBB2* and followed by the polyadenyl-

ation region of the same gene. The *COIN* element contains a *neo* selection cassette downstream of the *UBp* promoter and the *EM7* prokaryotic promoter and upstream of the poly-adenylation region of *Pgk1* flanked by flippase (FLP) recognition target (FRT) sequences (*Frt-neo-Pgk1polyA-Frt*) (Fig. 1*C*) (30–32). Prior to Cre recombination, the *COIN* module is removed by splicing of the precursor mRNA to generate a *Notch2COIN* transcript that is indistinguishable from the *Notch2WT* mRNA (Fig. 1*D*). In the presence of Cre recombinase, which recognizes the *lox71* and *lox66* mutant sites in a mirror image configuration, the *lox66_HA-egfp-polyA_lox71* cassette is brought into the sense strand, causing the irreversible conversion of the *COIN* allele. The resulting allele encodes for a bicistronic message that is translated into an HA-tagged Notch2 mutant truncated at lysine 2384 and thereby lacking the PEST domain and eGFP (Fig. 1*E*). This allele was termed *Notch2ΔPEST*.

To ensure skeletal equivalency of the *Notch2COIN* and *Notch2WT* alleles, the microarchitecture of the distal femur in 1-month-old *Notch2COIN/COIN* male and female mice and wild-type C57BL/6J controls of the same sex and age was analyzed. Cancellous bone volume and cortical thickness were not different between *Notch2COIN/COIN* mice and controls, demonstrating that homozygosity for the *Notch2COIN* allele has no appreciable effect on femoral microarchitecture (data not shown).

Inversion of the Notch2COIN allele in the germ line causes osteopenia

To validate the *Notch2COIN* mouse as a model of HCS, the skeletal phenotype of *Notch2ΔPEST/WT* mice created by inversion of the *COIN* module in the germ line was determined. To this end, *Notch2COIN/WT* male mice were crossed with *Hprt-Cre* female mice to create *Notch2ΔPEST/WT* mice; these were crossed with wild-type mice to create *Notch2ΔPEST/WT* heterozygous and control wild-type littermates. *COIN* inversion was documented by the presence of the *Notch2ΔPEST* allele in DNA from tails of *Notch2ΔPEST/WT* mice, and quantitative reverse transcription-polymerase chain reaction (qRT-PCR) analysis of total RNA from tibiae confirmed the expression of the *Notch2ΔPEST* transcript in mutant mice but not in control littermates (Fig. 2, *A* and *B*). *Notch2WT* transcript levels were ~50% lower in *Notch2ΔPEST/WT* mice than in wild-type littermates, and this is consistent with a systemic heterozygous *Notch2ΔPEST* inversion and comparable expression levels of the *Notch2ΔPEST* and Notch2WT alleles (Fig. 2*B*).

One-month-old germ line *Notch2ΔPEST/WT* male mice appeared normal, albeit a small reduction (~5%; $p < 0.05$) in femoral length was noted. Analysis of the distal femur by μCT revealed that, compared with sex-matched littermate controls, *Notch2ΔPEST/WT* male mice had a 50% decrease in trabecular bone volume secondary to a reduced number and thickness of trabeculae. Connectivity density was lower, and structure model index (SMI) was higher in *Notch2ΔPEST/WT* mice than in controls, indicating a prevalence of rod-like trabeculae (Table 1 and Fig. 2*C*). *Notch2ΔPEST/WT* mice had a thin and porous cortical bone, and their femurs were smaller than those from controls, because total area, bone area, and periosteal as well
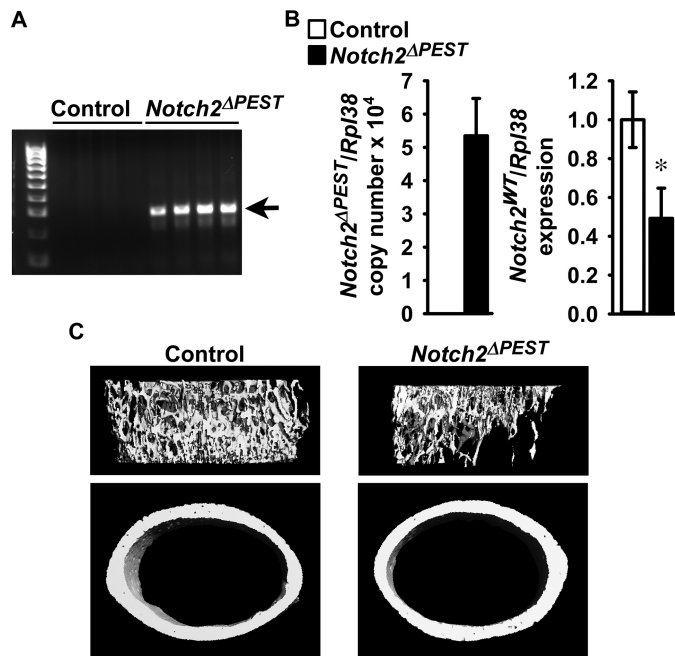

Figure 2. Inversion of the *Notch2COIN* allele in the germ line causes osteopenia. One-month-old male *Notch2ΔPEST/WT* mutants (*black bars*; *Notch2ΔPEST*) were compared with wild-type littermate controls (*white bars*) of the same sex. *A*, DNA was extracted from tail, and *Notch2COIN* inversion was documented by gel electrophoresis of PCR products obtained with primers specific for the *Notch2ΔPEST* allele. *Arrows* indicate the position of the 250-bp amplicon. *B*, total RNA was extracted from tibiae, and expression of the *Notch2ΔPEST* and *Notch2WT* mRNA was measured by qRT-PCR. Transcript levels are reported as copy number corrected for *Rpl38* mRNA levels; data for *Notch2WT* were normalized to corrected expression in control. Values are means ± S.D.; $n = 4$ for control, $n = 5$ for *Notch2ΔPEST*, all biological replicates. Two technical replicates were used for each qPCR. *, significantly different between control and *Notch2ΔPEST*, $p < 0.05$ by t test. *C*, representative μCT images of femoral proximal trabecular bone and midshaft cortical bones of control and *Notch2ΔPEST* mice; complete data set in Table 1.

Table 1

Femoral microarchitecture assessed by μCT of 1-month-old *Notch2ΔPEST/WT* (*Notch2ΔPEST*) mice and sex-matched wild-type littermates (control)

μCT was performed at the femoral distal end for trabecular or midshaft for cortical bone. Values are means ± S.D.

	Control	Notch2ΔPEST
Distal femur trabecular bone	$n = 4$	$n = 5$
Bone volume/total volume (%)	18.9 ± 2.1	9.8 ± 1.5[a]
Trabecular separation (μm)	134 ± 19	171 ± 13[a]
Trabecular no. (1/mm)	7.7 ± 1.0	5.9 ± 0.4[a]
Trabecular thickness (μm)	31 ± 1	25 ± 2[a]
Connectivity density (1/mm³)	1360 ± 152	720 ± 94[a]
Structure model index	1.6 ± 0.2	2.5 ± 0.1[a]
Density of material (mg HA/cm³)	923 ± 12	920 ± 27
Femoral midshaft cortical bone	$n = 4$	$n = 5$
Bone volume/total volume (%)	87.6 ± 0.5	85.6 ± 1.6[a]
Porosity (%)	12.4 ± 0.5	14.4 ± 1.6[a]
Cortical thickness (μm)	110 ± 5	97 ± 6[a]
Total area (mm²)	1.76 ± 0.10	1.50 ± 0.09[a]
Bone area (mm²)	0.59 ± 0.03	0.51 ± 0.04[a]
Periosteal perimeter (μm)	4.7 ± 0.1	4.3 ± 0.1[a]
Endocortical perimeter (mm)	3.8 ± 0.1	3.5 ± 0.1[a]
Density of material (mg HA/cm³)	1001 ± 11	999 ± 8

[a] Data are significantly different between control and *Notch2ΔPEST*, $p < 0.05$ by unpaired t test.

as endocortical perimeters were reduced (Table 1 and Fig. 2*C*). These results mirror the phenotype reported for global *Notch2HCS* mutants and validate the *Notch2COIN* mouse as a model to study the contribution of selected cell lineages

to the phenotypic manifestations of *Notch2HCS* mutant mice (27).

Inversion of the Notch2^COIN^ allele in the osteoclast lineage does not cause a skeletal phenotype

To establish whether the osteopenic phenotype of the *Notch2HCS* mutants is secondary to direct effects in cells of the osteoclast lineage, the *Notch2^COIN^* allele was introduced into *Lyz2^Cre/WT^* heterozygous mice. Subsequently, *Lyz2^Cre/WT^*; *Notch2^COIN/COIN^* mice were crossed with *Notch2^COIN/COIN^* mice for the creation of *Lyz2^Cre/WT^*;*Notch2^ΔPEST/ΔPEST^* experimental mice and *Notch2^COIN/COIN^* littermate controls. In an alternative mating scheme, the *Notch2^ΔPEST^* inversion was carried out in the context of *Lyz2^Cre^* homozygosity. To this end, *Lyz2^Cre/Cre^*;*Notch2^COIN/WT^* mice were crossed with *Lyz2^Cre/Cre^*; *Notch2^COIN/WT^* mice for the creation of *Lyz2^Cre/Cre^* *Notch2^ΔPEST/ΔPEST^* experimental and *Lyz2^Cre/Cre^*;*Notch2^WT/WT^* control mice. In preliminary studies, we documented that 1- and 4-month-old *Lyz2^Cre^* and 1-month-old *Lyz2^Cre/Cre^* mice did not have a skeletal phenotype as determined by μCT of distal femurs, when compared with wild-type controls (data not shown). *COIN* inversion was demonstrated in cultures of bone marrow-derived macrophages (BMMs) from 1-month-old *Lyz2^Cre/WT^*;*Notch2^ΔPEST/ΔPEST^* and *Lyz2^Cre/Cre^*;*Notch2^ΔPEST/ΔPEST^* mice, and expression of the *Notch2^ΔPEST^* mRNA was detected in total RNA from their parietal bones (Fig. 3, *A, B, D,* and *E*). These results demonstrate that the Hajdu-Cheney mutation was introduced and transcribed in *Lyz2*-expressing cells. Femoral microarchitecture of male and female at 1- or 4-month-old *Lyz2^Cre/WT^*;*Notch2^ΔPEST/ΔPEST^* mice or 1-month-old *Lyz2^Cre/Cre^*;*Notch2^ΔPEST/ΔPEST^* mice was not different from that of wild-type sex-matched littermate controls (Tables 2 and 3). In addition, BMM cultures from either *Lyz2^Cre/WT^*; *Notch2^ΔPEST/ΔPEST^* or *Lyz2^Cre/Cre^*;*Notch2^ΔPEST/ΔPEST^* mice and control littermates formed a similar number of osteoclasts *in vitro* (Fig. 3, *C* and *F*).

These results demonstrate that the induction of a dual *Notch2* mutant allele in cells of the osteoclastic lineage has no skeletal consequences and that the osteopenic phenotype of the global *Notch2HCS* mutant mice should be attributed to an effect in alternate cells (27).

Inversion of the Notch2^COIN^ allele in osteoblasts causes osteopenia

To determine whether the osteopenia observed in mice carrying the HCS mutation is driven by an effect in cells of the osteoblastic lineage, the *Notch2^ΔPEST^* mutation was created in *Bglap*-expressing cells. For this purpose, *BGLAP-Cre^+/−^*; *Notch2^COIN/COIN^* and *Notch2^COIN/COIN^* mice were crossed to create *BGLAP-Cre*;*Notch2^ΔPEST/ΔPEST^* mice and littermate *Notch2^COIN/COIN^* controls. As reported previously, *BGLAP-Cre* transgenics do not have a skeletal phenotype when compared with wild-type mice (15). Inversion of the *COIN* allele was detected in DNA from parietal bones of *BGLAP-Cre*; *Notch2^ΔPEST/ΔPEST^* mice at 1 and 4 months of age but not in littermate controls (Fig. 4*A*). Accordingly, the *Notch2^ΔPEST^* transcript was detected only in bones from *BGLAP-Cre*; *Notch2^ΔPEST/ΔPEST^* mice, documenting the induction of the
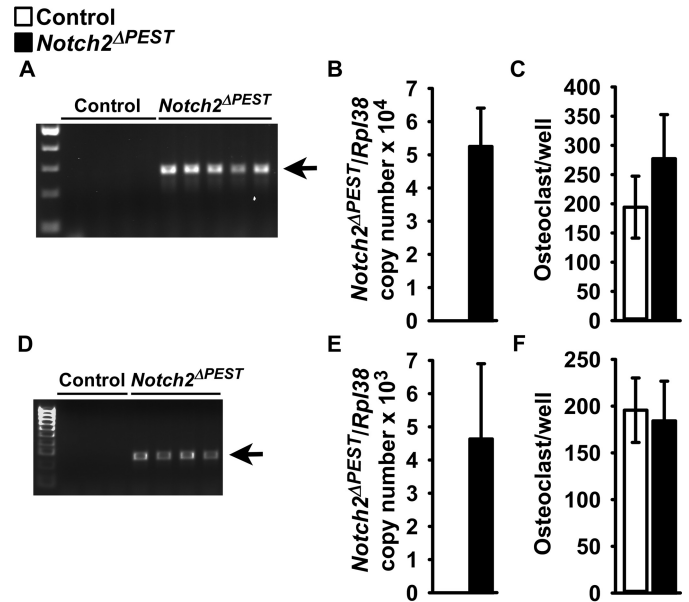
□ **Control**
■ ***Notch2^ΔPEST^***

Figure 3. Inversion of the *Notch2^COIN^* allele in *Lyz2*-expressing cells has no skeletal consequences. Documentation of *Notch2^COIN^* inversion, analysis of gene expression, and osteoclastogenesis in 1-month-old *Lyz2^Cre/WT^*; *Notch2^ΔPEST/ΔPEST^* or *Lyz2^Cre/Cre^*;*Notch2^ΔPEST/ΔPEST^* (*black bars*; *Notch2^ΔPEST^*) and sex-matched *Notch2^COIN/COIN^* or *Lyz2^Cre/Cre^*;*Notch2^WT/WT^* (*white bars*) controls, respectively. *A* and *D,* BMMs from 1-month-old *Lyz2^Cre/WT^*;*Notch2^ΔPEST/ΔPEST^* (*A*) or *Lyz2^Cre/Cre^*;*Notch2^ΔPEST/ΔPEST^* (*D*) mice and respective controls were cultured for 72 h in the presence of M-CSF at 30 ng/ml. DNA was extracted, and *Notch2^COIN^* inversion was demonstrated by gel electrophoresis of PCR products obtained with primers specific for the *Notch2^ΔPEST^* allele. The *arrows* indicate the position of the 250-bp amplicon. *B* and *E, Notch2^ΔPEST^* transcript levels were measured by qRT-PCR in total RNA from the parietal bones of *Lyz2^Cre/WT^*;*Notch2^ΔPEST/ΔPEST^* (*B*) or *Lyz2^Cre/Cre^*;*Notch2^ΔPEST/ΔPEST^* (*E*) mice and respective controls. Transcript levels are reported as copy number corrected for *Rpl38* mRNA levels. Values are means ± S.D.; *n* = 4–6 biological replicates. Values are means ± S.D.; *n* = 4 for both controls, *n* = 4 for *Lyz2^Cre/WT^*; *Notch2^ΔPEST/ΔPEST^*, *n* = 6 for *Lyz2^Cre/Cre^*;*Notch2^ΔPEST/ΔPEST^*, all biological replicates. Two technical replicates were used for each qPCR. *C* and *F,* BMMs from 1-month-old *Lyz2^Cre/WT^*;*Notch2^ΔPEST/ΔPEST^* (*C*) or *Lyz2^Cre/Cre^*;*Notch2^ΔPEST/ΔPEST^* (*F*) mice and respective controls were cultured for 72 h in the presence of M-CSF at 30 ng/ml and then with the addition of Rankl at 10 ng/ml until the formation of osteoclasts. Trap activity was assessed by enzyme histochemistry, and data are expressed as number of osteoclasts per well. Values are means ± S.D.; *n* = 4 for *Notch2^COIN/COIN^*, *n* = 3 for *Lyz2^Cre/Cre^*;*Notch2^WT/WT^*, *n* = 5 for *Lyz2^Cre/WT^*;*Notch2^ΔPEST/ΔPEST^*, and *n* = 4 for *Lyz2^Cre/Cre^*;*Notch2^ΔPEST/ΔPEST^*, all biological replicates.

HCS mutation in cells that express *BGLAP*. The presence of the *Notch2^ΔPEST^* mRNA was associated with increased transcript levels for *Hey1, Hey2,* and *HeyL,* demonstrating increased Notch2 signaling (Fig. 4*B*).

The general appearance, weight, and femoral length of 1- and 4-month-old *BGLAP-Cre*;*Notch2^ΔPEST/ΔPEST^* mice were not different from those of control sex-matched littermates (Fig. 5*A*). At 1 month of age, μCT revealed cancellous and cortical bone osteopenia in *BGLAP-Cre*;*Notch2^ΔPEST/ΔPEST^* female but not male mice. *BGLAP-Cre/Rpl38* copy number was (mean ± S.D.; *n* = 5–6) 1.6 ± 0.7 in male and 3.5 ± 1.2 (*p* < 0.05) in female littermates, possibly explaining the absence of a phenotype in *BGLAP-Cre*;*Notch2^ΔPEST/ΔPEST^* male mice. One month old *BGLAP-Cre*;*Notch2^ΔPEST/ΔPEST^* female mice had an ~50% reduction in cancellous bone volume secondary to a reduced number of trabeculae and connectivity density, associated with increased SMI, indicating a prevalence of rod-like over plate-like trabeculae. Cortical bone thickness and bone area were

Table 2

Femoral microarchitecture assessed by μCT of 1- and 4-month-old *Lyz2^Cre/WT^;Notch2^ΔPEST/ΔPEST^* (*Notch^ΔPEST^*) mice and sex-matched *Notch2^COIN/COIN^* littermates (control)

μCT was performed at the femoral distal end for trabecular or midshaft for cortical bone. Values are means ± S.D.

	1 Month		4 Months	
	Control	*Notch2^ΔPEST^*	Control	*Notch2^ΔPEST^*
Males				
Distal femur trabecular bone	$n = 4$	$n = 5$	$n = 4$	$n = 6$
Bone volume/total volume (%)	5.7 ± 1.8	6.8 ± 2.5	16.6 ± 3.8	15.9 ± 8.1
Trabecular separation (μm)	224 ± 36	213 ± 71	201 ± 18	214 ± 55
Trabecular no. (1/mm)	4.6 ± 0.7	5.0 ± 1.3	4.9 ± 0.4	4.8 ± 1.1
Trabecular thickness (μm)	24 ± 2	25 ± 1	45 ± 5	43 ± 4
Connectivity density (1/mm³)	306 ± 130	360 ± 191	228 ± 31	234 ± 120
Structure model index	2.8 ± 0.2	2.7 ± 0.2	1.2 ± 0.3	1.4 ± 1.0
Density of material (mg HA/cm³)	787 ± 13	798 ± 8	968 ± 29	968 ± 18
Femoral midshaft cortical bone	$n = 4$	$n = 5$	$n = 5$	$n = 5$
Bone volume/total volume (%)	84.0 ± 2.5	85.1 ± 1.3	99.6 ± 0.0	99.6 ± 0.2
Porosity (%)	16.0 ± 2.5	14.9 ± 1.3	0.4 ± 0.0	0.4 ± 0.2
Cortical thickness (μm)	84 ± 12	89 ± 8	169 ± 14	175 ± 9
Total area (mm²)	1.43 ± 0.17	1.49 ± 0.22	2.87 ± 0.79	3.54 ± 1.99
Bone area (mm²)	0.41 ± 0.07	0.44 ± 0.06	1.55 ± 0.47	2.26 ± 1.84
Periosteal perimeter (mm)	4.2 ± 0.3	4.3 ± 0.3	6.0 ± 0.8	6.5 ± 1.7
Endocortical perimeter (mm)	3.6 ± 0.2	3.6 ± 0.3	4.0 ± 0.5	4.0 ± 0.4
Density of material (mg HA/cm³)	952 ± 25	968 ± 8	1187 ± 19	1218 ± 23
Females				
Distal femur trabecular bone	$n = 4$	$n = 5$	$n = 5$	$n = 5$
Bone volume/total volume (%)	6.2 ± 1.5	5.8 ± 1.6	6.7 ± 1.4	5.4 ± 1.8
Trabecular separation (μm)	220 ± 21	226 ± 27	290 ± 16	298 ± 23
Trabecular no. (1/mm)	4.6 ± 0.5	4.5 ± 0.5	3.5 ± 0.2	3.4 ± 0.2
Trabecular thickness (μm)	25 ± 1	25 ± 1	42 ± 3	38 ± 4
Connectivity density (1/mm³)	263 ± 101	257 ± 97	117 ± 27	96 ± 55
Structure model index	2.7 ± 0.2	2.8 ± 0.2	2.6 ± 0.3	2.7 ± 0.4
Density of material (mg HA/cm³)	783 ± 15	781 ± 15	973 ± 15	971 ± 22
Femoral midshaft cortical bone	$n = 4$	$n = 4$	$n = 6$	$n = 4$
Bone volume/total volume (%)	82.7 ± 3.3	83.3 ± 3.0	99.5 ± 0.2	99.4 ± 0.2
Porosity (%)	17.3 ± 3.3	16.7 ± 3.0	0.5 ± 0.2	0.6 ± 0.2
Cortical thickness (μm)	83 ± 15	87 ± 10	170 ± 7	170 ± 4
Total area (mm²)	1.45 ± 0.10	1.56 ± 0.09	1.97 ± 0.13	2.10 ± 0.10
Bone area (mm²)	0.42 ± 0.07	0.45 ± 0.05	1.05 ± 0.07	1.17 ± 0.09
Periosteal perimeter (mm)	4.3 ± 0.1	4.4 ± 0.1	5.0 ± 0.2	5.1 ± 0.1
Endocortical perimeter (mm)	3.6 ± 0.1	3.7 ± 0.1	3.4 ± 0.1	3.4 ± 0.1
Density of material (mg HA/cm³)	960 ± 27	958 ± 29	1217 ± 15	1226 ± 20

Table 3

Femoral microarchitecture assessed by μCT of 1-month-old *Lyz2^Cre/Cre^;Notch2^ΔPEST/ΔPEST^* (*Notch2^ΔPEST^*) and *Notch2^COIN/COIN^* mice (control) of the same sex and age

μCT was performed at the femoral distal end for trabecular or midshaft for cortical bone. Values are means ± S.D.

	Males		Females	
1 Month	Control	*Notch2^ΔPEST^*	Control	*Notch2^ΔPEST^*
Distal femur trabecular bone	$n = 3$	$n = 4$	$n = 3$	$n = 3$
Bone volume/total Volume (%)	8.6 ± 3.2	7.6 ± 4.3	5.7 ± 1.3	9.6 ± 4.4
Trabecular separation (μm)	172 ± 31	194 ± 39	212 ± 18	175 ± 30
Trabecular no. (1/mm)	6.0 ± 1.1	5.3 ± 1.2	4.8 ± 0.4	5.9 ± 1.1
Trabecular thickness (μm)	27 ± 1	26 ± 3	26 ± 1	27 ± 4
Connectivity density (1/mm³)	376 ± 290	304 ± 328	176 ± 101	404 ± 337
Structure model index	2.8 ± 0.2	2.8 ± 0.1	2.7 ± 0.3	2.5 ± 0.1
Density of material (mg HA/cm³)	1011 ± 6	987 ± 15	979 ± 34	992 ± 16
Femoral midshaft cortical bone	$n = 3$	$n = 4$	$n = 3$	$n = 3$
Bone volume/total volume (%)	81.6 ± 3.9	84.1 ± 2.2	84.1 ± 0.6	85.6 ± 2.5
Porosity (%)	18.5 ± 3.9	15.9 ± 2.2	15.9 ± 0.6	14.4 ± 2.5
Cortical thickness (μm)	97 ± 13	105 ± 10	97 ± 6	111 ± 16
Total area (mm²)	1.55 ± 0.07	1. 51 ± 0.13	1.50 ± 0.17	1.55 ± 0.15
Bone area (mm²)	0.54 ± 0.03	0.53 ± 0.08	0.49 ± 0.01	0.57 ± 0.06
Periosteal perimeter (mm)	4.4 ± 0.1	4.3 ± 0.2	4.3 ± 0.2	4.4 ± 0.2
Endocortical perimeter (mm)	3.6 ± 0.1	3.5 ± 0.1	3.5 ± 0.3	3.5 ± 0.3
Density of material (mg HA/cm³)	1047 ± 3	1066 ± 7	1061 ± 14	1077 ± 49

decreased in female mutant mice, and cortical bone was porous (Fig. 5*B* and Table 4). At 4 months of age, the skeletal phenotype of *BGLAP-Cre;Notch2^ΔPEST/ΔPEST^* female mice was less pronounced, and cancellous bone volume/total volume was 30% lower than in control littermates ($p < 0.071$). A modest cortical osteopenia with cortical thinning and increased porosity was observed in *BGLAP-Cre;Notch2^ΔPEST/ΔPEST^* 4-month-old mice of both sexes (Fig. 6*B* and Table 4).

Cancellous bone histomorphometry of the distal femur of 1-month-old female *BGLAP-Cre;Notch2^ΔPEST/ΔPEST^* mice confirmed the decreased bone volume/tissue volume secondary to a reduced number of trabeculae. Eroded surface and osteoclast numbers were increased, whereas the numbers of osteoblasts and bone formation rates were not different from control littermates (Table 5). Cortical bone histomorphometry revealed a suppressed endocortical mineral
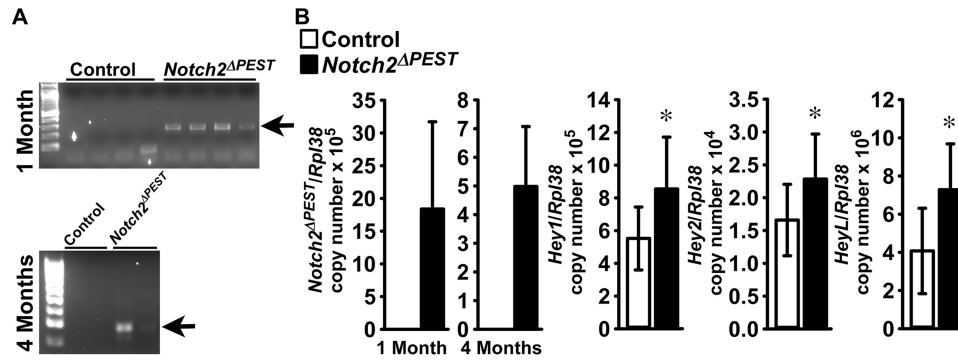
Figure 4. Inversion of the *Notch2^COIN* allele in osteoblasts leads to *Notch2* activation *in vivo*. Documentation of *Notch2^COIN* inversion and analysis of gene expression in *BGLAP-Cre;Notch2^{ΔPEST/ΔPEST}* (*black bars*; *Notch2^{ΔPEST}*) and *Notch2^{COIN/COIN}* littermate controls (*white bars*). *A*, DNA was extracted from the parietal bones of 1- and 4-month-old male mice, and *Notch2^COIN* inversion was demonstrated by gel electrophoresis of PCR products obtained with primers specific for the *Notch2^{ΔPEST}* allele. The *arrows* indicate the position of the 250-bp amplicon. *B*, gene expression was measured by qRT-PCR in total RNA from tibiae of 4-month-old mice. Transcript levels are reported as *Notch2^{ΔPEST}*, *Hey1*, *Hey2*, and *HeyL* mRNA copy number corrected for *Rpl38* expression. Values are means ± S.D.; $n = 11$ biological replicates for both groups. Two technical replicates were used for each qPCR. *, significantly different between *Notch2^{ΔPEST}* and control, $p < 0.05$ by *t* test.
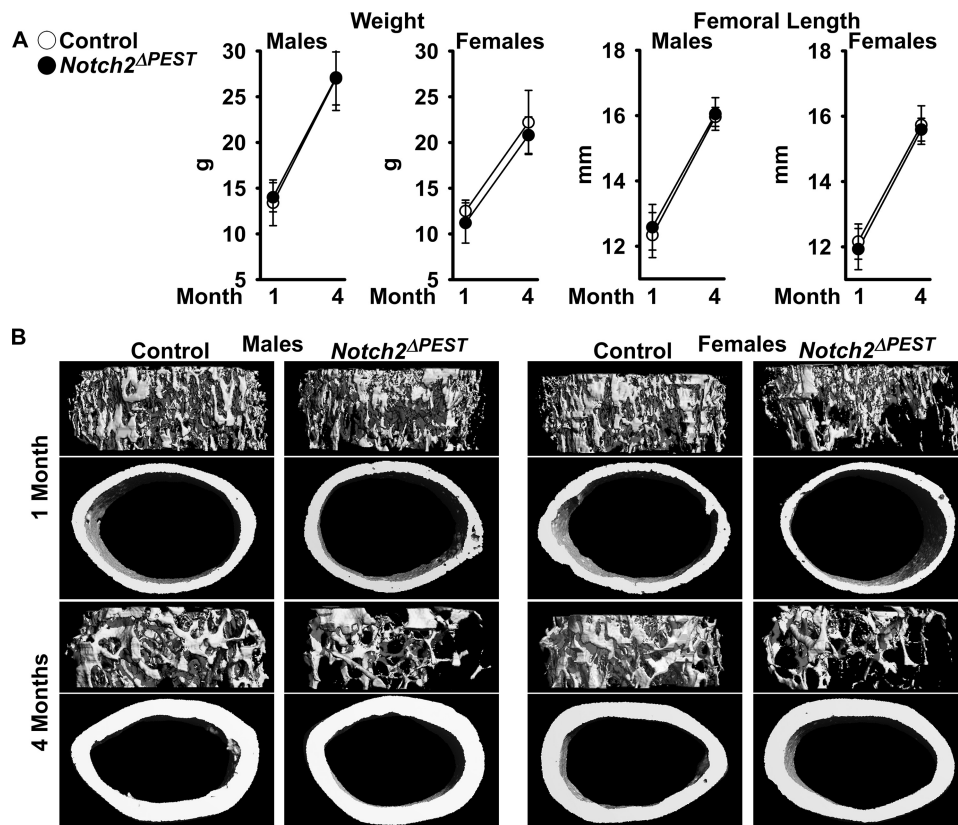

Figure 5. Notch2 activation in osteoblasts causes osteopenia. One- and 4-month-old male and female *BGLAP-Cre;Notch2^{ΔPEST/ΔPEST}* (*black dots*; *Notch2^{ΔPEST}*) were compared with sex-matched littermate *Notch2^{COIN/COIN}* controls (*open circles*). *A*, weight and femoral length. Values are means ± S.D.; in males at 1 month of age $n = 7$ for control, $n = 12$ for *Notch2^{ΔPEST}*, and at 4 months of age $n = 6$ for control, $n = 6$ for *Notch2^{ΔPEST}*; in females at 1 month of age $n = 7$ for control, $n = 7$ for *Notch2^{ΔPEST}*, and at 4 months of age $n = 5$ for control, $n = 6$ for *Notch2^{ΔPEST}*, all biological replicates. *B*, representative μCT images of femoral proximal trabecular bone and midshaft. Complete data set in Table 4.

apposition rate in *BGLAP-Cre;Notch2^{ΔPEST/ΔPEST}* mice (Table 6).

Inversion of the Notch2^COIN allele in osteoblasts induces Tnfsf11

To determine the mechanisms responsible for the skeletal phenotype of the *BGLAP-Cre;Notch2^{ΔPEST/ΔPEST}* mice, osteoblast-enriched cells were obtained from the parietal bones of *Notch2^{COIN/COIN}* newborns. Cultures were infected with an

adenoviral vector expressing Cre recombinase under the control of the cytomegalovirus (CMV) promoter, and parallel cultures infected with an adenoviral vector where the CMV promoter governs GFP expression (Ad-CMV-GFP) served as controls. Ad-CMV-Cre, but not Ad-CMV-GFP, infection led to the inversion of the *COIN* module and expression of the *Notch2^{ΔPEST}* mRNA associated with induction of *Hey1* and *HeyL*, demonstrating activation of Notch signaling (Fig. 6, *A* and *B*). In accordance with the enhanced bone resorption

Table 4

Femoral microarchitecture assessed by μCT of 1- and 4-month-old *BGLAP-Cre;Notch2$^{\Delta PEST/\Delta PEST}$* (*Notch2$^{\Delta PEST}$*) mice and sex-matched *Notch2$^{COIN/COIN}$* littermates (control)

μCT was performed at the femoral distal end for trabecular or midshaft for cortical bone. Values are means $\pm$ S.D.

	1 Month		4 Months	
	Control	*Notch2$^{\Delta PEST}$*	Control	*Notch2$^{\Delta PEST}$*
Males				
Distal femur trabecular bone	$n = 7$	$n = 12$	$n = 6$	$n = 6$
Bone volume/total volume (%)	10.0 ± 4.4	10.4 ± 5.5	13.3 ± 2.5	11.7 ± 2.8
Trabecular separation (μm)	176 ± 32	186 ± 29	207 ± 30	226 ± 48
Trabecular no. (1/mm)	5.9 ± 1.0	5.6 ± 0.9	4.9 ± 0.7	4.6 ± 0.9
Trabecular thickness (μm)	28 ± 4	29 ± 6	44 ± 5	40 ± 3
Connectivity density (1/mm^3)	500 ± 262	532 ± 224	341 ± 124	361 ± 159
Structure model index	2.6 ± 0.5	2.4 ± 0.5	2.0 ± 0.2	2.1 ± 0.3
Density of material (mg HA/cm^3)	799 ± 15	791 ± 11	941 ± 10	927 ± 11[a]
Femoral midshaft cortical bone	$n = 7$	$n = 12$	$n = 6$	$n = 6$
Bone volume/total volume (%)	83.7 ± 2.9	83.6 ± 1.5	88.5 ± 1.0	87.0 ± 0.9[a]
Porosity (%)	16.3 ± 2.9	16.5 ± 1.5	11.5 ± 1.0	13.0 ± 0.9[a]
Cortical thickness (μm)	95 ± 13	93 ± 14	179 ± 7	158 ± 9[a]
Total area (mm^2)	1.52 ± 0.14	1.65 ± 0.16	2.2 ± 0.2	2.2 ± 0.3
Bone area (mm^2)	0.48 ± 0.07	0.51 ± 0.10	1.00 ± 0.08	1.03 ± 0.33
Periosteal perimeter (mm)	4.4 ± 0.2	4.5 ± 0.2	5.2 ± 0.2	5.3 ± 0.4
Endocortical perimeter (mm)	3.6 ± 0.1	3.8 ± 0.1[a]	3.8 ± 0.2	3.9 ± 0.4
Density of material (mg HA/cm^3)	967 ± 27	961 ± 29	1198 ± 12	1182 ± 11[a]
Females				
Distal femur trabecular bone	$n = 7$	$n = 7$	$n = 5$	$n = 6$
Bone volume/total volume (%)	9.3 ± 3.0	4.3 ± 2.3[a]	5.7 ± 1.0	4.0 ± 1.7[b]
Trabecular separation (μm)	175 ± 32	293 ± 56[a]	309 ± 37	377 ± 64[b]
Trabecular no. (1/mm)	5.9 ± 1.0	3.6 ± 0.8[a]	3.3 ± 0.4	2.8 ± 0.5[b]
Trabecular thickness (μm)	27 ± 1	25 ± 4	43 ± 3	39 ± 4[b]
Connectivity density (1/mm^3)	517 ± 244	187 ± 178[a]	103 ± 32	79 ± 45
Structure model index	2.6 ± 0.2	3.0 ± 0.3[a]	2.7 ± 0.1	2.7 ± 0.3
Density of material (mg HA/cm^3)	791 ± 11	782 ± 11[a]	947 ± 16	921 ± 13[a]
Femoral midshaft cortical bone	$n = 7$	$n = 7$	$n = 5$	$n = 6$
Bone volume/total volume (%)	83.3 ± 1.3	79.6 ± 3.2[a]	87.6 ± 1.1	86.3 ± 0.7[a]
Porosity (%)	16.7 ± 1.3	20.4 ± 3.2[a]	12.4 ± 1.1	13.7 ± 0.7[a]
Cortical thickness (μm)	93 ± 7	78 ± 8[a]	171 ± 16	152 ± 7[a]
Total area (mm^2)	1.54 ± 0.15	1.44 ± 0.18	1.73 ± 0.14	1.60 ± 0.07
Bone area (mm^2)	0.48 ± 0.06	0.40 ± 0.05[a]	0.85 ± 0.12	0.74 ± 0.05[b]
Periosteal perimeter (mm)	4.4 ± 0.2	4.2 ± 0.3	4.7 ± 0.2	4.5 ± 0.1
Endocortical perimeter (mm)	3.7 ± 0.2	3.6 ± 0.2	3.3 ± 0.1	3.3 ± 0.1
Density of material (mg HA/cm^3)	965 ± 29	941 ± 34	1235 ± 7	1211 ± 15[a]

[a] Data are significantly different between control and *Notch2$^{\Delta PEST}$*, $p < 0.05$ by unpaired t test.
[b] $p < 0.071$ done by unpaired t test.

observed in *BGLAP-Cre;Notch2$^{\Delta PEST/\Delta PEST}$* mice, expression of *Tnfsf11* was induced in *Notch2$^{\Delta PEST}$* cells (27).

Discussion

In this study, the individual contributions of the osteoclast and osteoblast lineages to the bone loss observed in *Notch2HCS* mutant mice were explored by the conditional introduction of the HCS genetic defect in selected cell lineages. The mutations associated with the disease occur within exon 34 of *NOTCH2*, and conditional insertion of a premature STOP codon in the homologous region of the murine *Notch2* locus was achieved by the creation of a *COIN* allele. The *COIN* module can be introduced directly into coding exons without disrupting the expression or function of the targeted allele, a goal that cannot be accomplished with traditional Cre-*loxP* approaches (28). Absence of an appreciable phenotype in *Notch2$^{COIN/COIN}$* mice documented the skeletal equivalency of the wild-type and engineered *Notch2* alleles prior to Cre-mediated inversion. The *Notch2$^{\Delta PEST}$* mutants generated by germ line inversion of the *COIN* module expressed the *Notch2$^{\Delta PEST}$* transcript and exhibited a 50% reduction in wild-type *Notch2* mRNA, indicating comparable expression levels of maternal and paternal *Notch2*. *Notch2$^{\Delta PEST}$* germ line mice exhibited generalized osteopenia and reduced bone size and length, phenocopying global *Notch2HCS* mutants. These results validated the COIN strat-

egy and confirmed that generalized expression of a *Notch2* mutant lacking the PEST domain causes bone loss (27). Although these findings should be extrapolated with caution to the human condition, they support the concept that *de novo* or inherited dominant *NOTCH2* gain-of-function mutations are responsible for the bone loss in subjects with HCS (33).

Selective introduction of the HCS mutation in osteoblasts, but not in cells of the myeloid lineage, led to generalized bone loss. The reduction in cancellous bone volume was observed only in female mice and was more pronounced in younger *BGLAP-Cre;Notch2$^{\Delta PEST/\Delta PEST}$* mice. The bone loss was attributed to enhanced bone resorption uncoupled from a bone-forming response and suppressed endocortical bone formation. These features are consistent with the skeletal phenotype of global *Notch2HCS* mutants and demonstrate that a direct effect in osteoblasts is largely responsible for the osteopenia associated with the HCS mutation in mice (27). Absence of a phenotype in *Lyz2$^{Cre/WT}$;Notch2$^{\Delta PEST/\Delta PEST}$* and *Lyz2$^{Cre/Cre}$; Notch2$^{\Delta PEST/\Delta PEST}$* mice is congruent with the observation that the *Notch2* deletion in *Lyz2*-expressing cells has no consequences on skeletal homeostasis (18). These results indicate that either the activation or inactivation of *Notch2* in myeloid cells *in vivo* has no skeletal consequences and that the effect of Notch2 on bone resorption is secondary to its actions on alter-
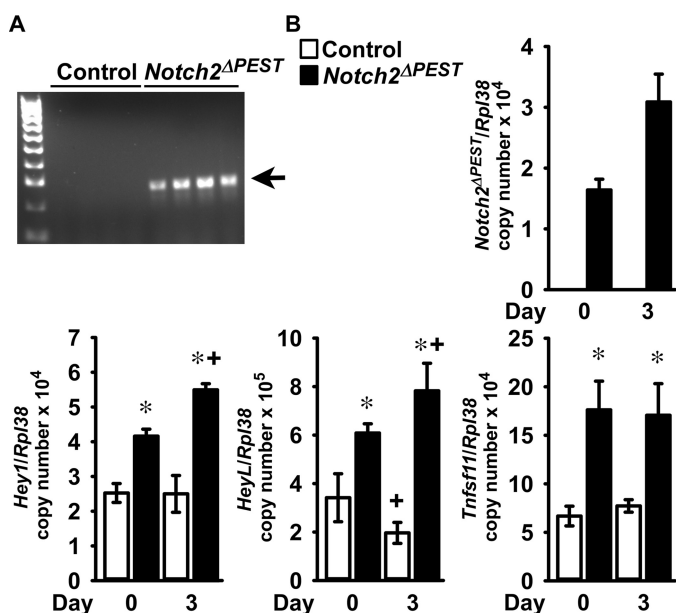
Figure 6. Notch2 activation in osteoblasts induces *Tnfsf11* expression. Calvarial osteoblast-enriched cells from 3- to 5-day-old *Notch2*$^{COIN/COIN}$ mice of both sexes were infected with Ad-CMV-Cre (*Notch2*$^{\Delta PEST}$; *black bars*) or Ad-CMV-GFP (control, *white bars*). *A*, DNA was extracted, and *Notch2*^{COIN} inversion was documented by gel electrophoresis of PCR products obtained with primers specific for the *Notch2*$^{\Delta PEST}$ allele. The *arrow* indicates the position of the 250-bp amplicon. *B*, total RNA was extracted, and gene expression was measured by qRT-PCR in the presence of specific primers. Transcript levels are reported as *Notch2*$^{\Delta PEST}$, *Hey1*, *HeyL*, and *Tnfsf11*, corrected for *Rpl38* expression. Values are means ± S.D.; $n = 4$ for all groups, all technical replicates from the same cell preparation. Two technical replicates were used for each qPCR. *, significantly different between *Notch2*$^{\Delta PEST}$ and control, $p < 0.05$; +, significantly different from day 0, $p < 0.05$; two-way analysis of variance with Holm-Šídák post-hoc analysis.

Table 5

Cancellous bone histomorphometry of 1-month-old *BGLAP-Cre*; *Notch2*$^{\Delta PEST/\Delta PEST}$ (*Notch2*$^{\Delta PEST}$) female mice and sex-matched *Notch2*$^{COIN/COIN}$ littermates (control)

Histomorphometry was carried out on sagittal sections of the distal femur. Values are means ± S.D.

Distal femur trabecular bone	Control	Notch2$^{\Delta PEST}$
Static histomorphometry	$n = 6$	$n = 5$
Bone volume/tissue volume (%)	11.1 ± 1.8	6.2 ± 1.3^a
Trabecular separation (μm)	274 ± 57	542 ± 348
Trabecular no. (1/mm)	3.4 ± 0.7	2.2 ± 0.9^a
Trabecular thickness (μm)	34 ± 7	32 ± 11
Osteoblast surface/bone surface (%)	13.0 ± 6.0	15.5 ± 10.3
Osteoblasts/bone perimeter (1/mm)	12.0 ± 5.1	13.5 ± 8.2
Osteoid surface/bone surface (%)	1.4 ± 1.4	1.4 ± 1.9
Osteoclast surface/bone surface (%)	17.2 ± 3.8	27.0 ± 9.3^a
Osteoclasts/bone perimeter (1/mm)	5.8 ± 1.0	9.8 ± 3.8^a
Eroded surface/bone surface (%)	8.2 ± 1.4	14.2 ± 4.2^a
Dynamic histomorphometry	$n = 3$	$n = 3$
Mineral apposition rate (μm/day)	2.8 ± 1.1	2.5 ± 0.5
Mineralizing surface/bone surface (%)	2.5 ± 1.0	4.0 ± 2.2
Bone formation rate (μm^3/μm^2/day)	0.08 ± 0.05	0.11 ± 0.07

^{a} Data are significantly different between control and *Notch2*$^{\Delta PEST}$, $p < 0.05$ by unpaired *t* test.

Table 6

Cortical bone histomorphometry of 1-month-old *BGLAP-Cre*; *Notch2*$^{\Delta PEST/\Delta PEST}$ (*Notch2*$^{\Delta PEST}$) female mice and sex-matched *Notch2*$^{COIN/COIN}$ littermates (control)

Cortical bone histomorphometry was performed at the femoral mid-diaphysis. Values are means ± S.D.

	Control	Notch2$^{\Delta PEST}$
Cortical bone	$n = 6$	$n = 6$
Cortical thickness (μm)	199 ± 19	190 ± 23
Bone area (mm^2)	0.48 ± 0.04	0.45 ± 0.08
Endocortical surface		
Static histomorphometry	$n = 6$	$n = 6$
Osteoblasts/bone perimeter (1/mm)	10.3 ± 5.0	6.0 ± 2.3
Osteoclasts/bone perimeter (1/mm)	2.4 ± 0.6	2.7 ± 0.7
Eroded surface/bone surface (%)	3.9 ± 0.9	4.1 ± 0.9
Dynamic histomorphometry	$n = 4$	$n = 5$
Mineral apposition rate (μm/day)	2.5 ± 0.3	1.7 ± 0.2^a

^{a} Data are significantly different between control and *Notch2*$^{\Delta PEST}$, $p < 0.05$ by unpaired *t* test.

mice, *Notch2*$^{\Delta PEST/\Delta PEST}$ osteoblasts expressed increased levels of *Tnfs11* mRNA suggesting that osteoblast-derived Rankl is responsible for the enhanced bone resorption *in vivo* in *HCS* mutant mice. These findings are in agreement with those in a subject with HCS and severe osteoporosis who was reported to present with elevated levels of circulating RANKL (27, 35). However, a limitation of this work was the inability to detect Rankl protein by Western blot analysis in either control or *Notch2*$^{\Delta PEST/\Delta PEST}$ osteoblasts. This is possibly related to low levels of Rankl expression and the lack of available antibodies with sufficient sensitivity to detect murine Rankl in osteoblasts. There was an absence of a bone-forming response to the increased bone resorption implying that Notch2 inhibits bone formation. Moreover, *Notch2* gain-of-function suppresses endocortical mineral apposition rate, an effect that possibly contributes to the cortical osteopenic phenotype. The role of Notch2 as an inhibitor of bone formation is supported by previous studies demonstrating that deletion of *Notch2* in *Runx2*-expressing cells increases trabecular bone volume due to enhanced osteoblast differentiation and activity (18). Further support for an inhibitory role of Notch2 on bone formation is derived from studies showing that the dual inactivation of *Notch1* and *Notch2* in cells of the osteoblastic lineage increases bone mass (36, 37).

It is important to mention that some discrepancies exist between the phenotypes of the *BGLAP-Cre*;*Notch2*$^{\Delta PEST/\Delta PEST}$ mice and of the global *Notch2HCS* mutants (27). The osteoblast-selective mutation did not affect femoral length, and this was expected because the *BGLAP-Cre* transgene is not expressed in chondrocytes, cells that govern longitudinal bone growth. Direct inhibitory effects of Notch2 on endochondral bone formation are accountable for the reduced femoral length of the *Notch2HCS* mutants (38, 39). Cancellous bone osteopenia was detected only in female *BGLAP-Cre*;*Notch2*$^{\Delta PEST/\Delta PEST}$ mice, although both sexes were affected by the global *Notch2HCS* mutation (27). These sex-related differences may be secondary to the more pronounced expression of the *BGLAP-Cre* transgene in female than in male mice. Alternatively, a higher rate of bone remodeling in young female than in male mice, a known attribute of the C57BL/6 genetic background, might have sensitized female mice to a greater activation of *Notch2* in osteoblasts (40, 41). The cortical bone

nate cells (17, 27, 34). However, the *in vivo* observations are in contrast with *in vitro* studies demonstrating that Notch2 enhances osteoclastogenesis directly and as a result bone resorption (17). This would suggest that the overall effect of Notch2 in osteoclastogenesis is complex and derived from its actions in various cellular lineages.

In agreement with previous work demonstrating increased expression of *Tnfs11* in bone extracts from *Notch2HCS* mutant

osteopenia was milder in *BGLAP-Cre;Notch2$^{\Delta PEST/\Delta PEST}$* than in the *Notch2HCS* mice, and low expression of the *BGLAP-Cre* transgene during embryonic skeletal development might account for the less pronounced phenotype of the conditional mice (42). It is of interest that the *BGLAP-Cre; Notch2$^{\Delta PEST/\Delta PEST}$* mice did not display the increase in endocortical bone resorption observed in the global *Notch2HCS* mutants. This difference may also account for the modest cortical bone phenotype of the conditional mice and suggests that the presence of the HCS mutation in both osteoclasts and osteoblasts might be necessary to recapitulate the cortical bone-resorptive phenotype and osteopenia of the *Notch2HCS* mouse (27).

The conditional HCS model described in this study reaffirmed that Notch2, like Notch1, increases the transcript levels of *Hey1*, *Hey2*, and *HeyL*, thereby confirming that both paralogs are able to activate Rbpjκ-mediated Notch signaling in skeletal cells. The increase in mRNA levels for the Notch target genes reflects activation of the Notch canonical pathway but does not imply that Hey proteins mediate the effects of Notch2 in bone. In fact, either generalized or skeletal misexpression of *Heys* has a small impact on skeletal microarchitecture (43–46). The current observations also indicate that Notch1 and Notch2 have distinct skeletal functions because Notch1 induces osteoprotegerin and inhibits bone resorption, whereas Notch2 induces Rankl and stimulates the resorptive event.

In conclusion, osteoblast expression of a *Notch2* mutant lacking the PEST domain causes osteopenia in mice.

Experimental procedures

Creation of the Notch2^{COIN} mouse

The targeting vector containing the *COIN* element was electroporated into embryonic stem (ES) cells, and the cassette was used for the selection of G418-resistant cells from 129SvJ/ C57BL/6J embryos at the Gene Targeting and Transgenic Facility of UConn Health. Targeted clones were verified by long-range PCR of genomic DNA. Correct integration of the 5′-homology arm was tested with forward F1 5′-GGGAGGT-GCTTACCGACCTCTC-3′ and reverse R1 5′-CACCCT-GAAAACTTTGCCCCCTCC-3′ primers followed by nested forward F2 5′-CTGTTCTTGGATACCGAGGTACAC-3′ and reverse R2 5′-CAATCAAGGGTCCCCAAACTCAC-3′ primers. Proper integration of the 3′-homology arm was ensured with forward F3 5′-CCAAAACCCGGCGCGGAGGC-CATGC-3′ and reverse R3 5′-CACTTGAGAGCAAGGCTG-CAAGGC-3′ primers followed by nested forward F4 5′-CCTTCTTCTCTTTCCTACAGTACCCC-3′ and reverse R4 5′-GGTGCAAGGGCAGGAGATCAACAG-3′ primers (all primers from Integrated DNA Technologies, IDT, Coralville, IA). Positive ES clones were used for morula aggregations and the creation of chimeras, and the *Frt-neo-Pgk1polyA-Frt* cassette was removed by FLP recombination following crosses of male chimeras with mice expressing FLP under the control of the *Rosa26* promoter (*Rosa26^{FLP}*; The Jackson Laboratory, Bar Harbor, ME) (47, 48). Excision of the cassette was verified by PCR in ear punches of F1 pups, and the *Rosa26^{FLP}* allele segregated by breeding with C57BL/6J wild-type mice.

Correct integration of the COIN module into the *Notch2* locus was confirmed in the progeny by loss of wild-type allele assay.

Induction of the HCS mutation in the germ line, osteoclasts, or osteoblasts

To test whether the *Notch2^{COIN}* and *Notch2^{WT}* alleles are functionally equivalent, the skeletal phenotype of *Notch2$^{COIN/COIN}$* mice was compared with the phenotype of wild-type C57BL/6J controls of the same age and sex. To achieve systemic inversion of the *Notch2^{COIN}* allele, F1 heterozygous *Notch2$^{COIN/WT}$* male mice were bred with female mice expressing Cre under the control of the *Hprt* promoter (*Hprt^{Cre}*) (49). This resulted in the germ line inversion of the *COIN* module and consequent creation of mice heterozygous for the *Notch2$^{\Delta PEST}$* allele (*Notch2$^{\Delta PEST/WT}$*). The latter were crossed with wild-type C57BL/6J mice to generate *Notch2$^{\Delta PEST/WT}$* experimental and wild-type control cohorts.

C57BL/6J mice where the Cre coding sequence was inserted into the endogenous *Lyz2* locus (*Lyz2^{Cre}*; The Jackson Laboratory) were used to express Cre recombinase in cells of the myeloid lineage (50, 51). To induce inversion of the *COIN* module in osteoclast precursor, homozygous *Notch2^{COIN}* mice heterozygous for the *Lyz2^{Cre}* allele (*Lyz2$^{Cre/WT}$*; *Notch2$^{COIN/COIN}$*) were bred with *Notch2$^{COIN/COIN}$* mice to create *Lyz2$^{Cre/WT}$*; *Notch2$^{\Delta PEST/\Delta PEST}$* mice. In an alternate mating scheme, heterozygous *Notch2^{COIN}* mice homozygous for the *Lyz2^{Cre}* allele (*Lyz2$^{Cre/Cre}$*;*Notch2$^{COIN/WT}$*) were inter-mated to create *Lyz2$^{Cre/Cre}$*;*Notch2$^{\Delta PEST/\Delta PEST}$* experimental and *Lyz2$^{Cre/Cre}$*; *Notch2$^{WT/WT}$* control mice.

C57BL/6J mice harboring a transgene where the Cre recombinase coding sequence was cloned downstream a 3.9-kb human *BGLAP* promoter fragment (*BGLAP-Cre*; The Jackson Laboratory) were used to induce inversion of the *COIN* module in osteoblasts (42). Hemizygous *BGLAP-Cre* transgenics homozygous for the *Notch2^{COIN}* allele (*BGLAP-Cre; Notch2$^{COIN/COIN}$*) were bred with *Notch2$^{COIN/COIN}$* mice to generate *BGLAP-Cre;Notch2$^{\Delta PEST/\Delta PEST}$* experimental and *Notch2$^{COIN/COIN}$* littermate control cohorts.

Allelic composition was determined by PCR analysis in tail DNA with primers specific for the *Hprt^{WT}*, *Hprt^{Cre}*, *Notch2^{WT}*, *Notch2^{COIN}*, *Notch2$^{\Delta PEST}$*, *Lyz2^{Cre}*, and *Lyz2^{WT}* alleles and for the *BGLAP-Cre* transgene. Inversion of the *COIN* module was documented by PCR analysis in DNA from BMMs or parietal bones (all primers were from IDT; Table 7). The generation and establishment of the *Notch2^{COIN}* mouse line were approved by the Institutional Animal Care and Use Committees of UConn Health and of Saint Francis Hospital Medical Center. All other studies were approved by the Institutional Animal Care and Use Committee of UConn Health.

Microcomputed tomography

Femoral microarchitecture was determined using a microcomputed tomography instrument (Scanco μCT 40; Scanco Medical AG, Bassersdorf, Switzerland), which was calibrated periodically using a phantom provided by the manufacturer (41, 52). Femurs were scanned in 70% ethanol at high resolution, energy level of 55 peak kV, intensity of 145 μA, and inte-

Table 7
Primers used for genotyping and determination of the COIN module inversion by PCR

Allele	Strand	Sequence 5′–3′	Amplicon size (bp)
$Notch2^{COIN}$	Forward	CCGGGCCGCGACTGAAACCCTAG	330
	Reverse	CCACCACCTCCAGGAGTTGGGC	
$Notch2^{WT}$	Forward	GCTCAGACCATTGTGCCAACCTAT	100
	Reverse	CAGCAGCATTTGAGGAGGCGTAA	
$Hprt^{WT}$	Forward	TTTCTATAGGACTGAAAGACTTGCTC	200
	Reverse	CACAGTAGCTCTTCAGTCTGATAAAA	
$Hprt^{Cre}$	Forward	GCGGTCTGGCAGTAAAAACTATC	100
	Reverse	GTGAAACAGCATTGCTGTCACTT	
$Lyz2^{Cre}$	Forward1	TTACAGTCGGCCAGGCTGAC	$Lyz2^{WT}$ = 350
	Forward2	CCCAGAAATGCCAGATTACG	$Lyz2^{Cre}$ = 700
	Reverse	CTTGGGCTGCCAGAATTTCTC	
BGLAP-Cre	Forward	CAAATAGCCCTGGCAGAT	300
	Reverse	TGATACAAGGGACATCTTCC	
Fabp1	Forward	TGGACAGGACTGGACCTCTGCTTTCC	200
	Reverse	TAGAGCTTTGCCACATCACAGGTCAT	
$Notch2^{\Delta PEST}$	Forward	GTACTTCAGCACAGTTTTAGAGAAC	250
	Reverse	GTGAGTCACCCGCCGGATGTC	

gration time of 200 ms. A total of 100 slices at midshaft and 160 slices at the distal metaphysis was acquired at an isotropic voxel size of 216 μm^3 and a slice thickness of 6 μm and chosen for analysis. Trabecular bone volume fraction (bone volume/total volume) and microarchitecture were evaluated starting ~1.0-mm proximal from the femoral condyles. Contours were manually drawn every 10 slices, a few voxels away from the endocortical boundary, to define the region of interest for analysis, whereas the remaining slice contours were iterated automatically. Total volume, bone volume, bone volume fraction, trabecular thickness, trabecular number, connectivity density, SMI, and material density were measured in trabecular regions using a Gaussian filter ($\sigma = 0.8$) and user-defined thresholds (41, 52). For analysis of cortical bone, contours were iterated across 100 slices along the cortical shell of the femoral midshaft, excluding the marrow cavity. Analysis of bone volume/total volume, porosity, cortical thickness, total cross-sectional and cortical bone area, periosteal and endosteal perimeter, and material density were conducted using a Gaussian filter ($\sigma = 0.8$, support = 1) with operator-defined thresholds.

Bone histomorphometric analysis

Bone histomorphometry was carried out in 1-month-old mice injected with 20 mg/kg calcein and 50 mg/kg demeclocycline at a 2-day interval and sacrificed 2 days after demeclocycline administration. Femurs were dissected, fixed in 70% ethanol, and embedded in methyl methacrylate. For cancellous bone analysis, bones were sectioned at a thickness of 5 μm along the sagittal plane on a Microm microtome (Richards-Allan Scientific, Kalamazoo, MI) and stained with 0.1% toluidine blue. Static and dynamic parameters of bone morphometry were measured in a defined area between 0.35 and 2.16 mm from the growth plate at a magnification of $\times100$ using an OsteoMeasure morphometry system (Osteometrics, Atlanta, GA). Stained sections were used to draw the bone and to measure trabecular separation, number, and thickness, osteoid and eroded surface, as well as to count osteoblast and osteoclast surface and number. Mineralizing surface per bone surface and

mineral apposition rate were measured on unstained sections visualized under UV light and a triple diamidino-2-phenylindole/fluorescein/Texas Red set long pass filter, and bone formation rate was calculated.

For cortical histomorphometry, femurs were embedded in methyl methacrylate and cut through the mid-diaphysis along the transverse plane with an EXAKT Precision Saw, ground using an EXAKT 400 CS Micro Grinding System (Exakt Technologies, Oklahoma City, OK), and surface-polished to a thickness of ~15 μm (Alizee Pathology, Baltimore, MD). Parameters of cortical bone morphometry were measured at a magnification of $\times400$ using OsteoMeasureXP software (Osteometrix). Stained sections were used to draw the cortical bone, marrow space, and cell surfaces, as well as to measure osteoblasts and osteoclasts along the endocortical surface. Mineral apposition rate was measured in unstained sections under UV light, using a triple diamidino-2-phenylindole/fluorescein/Texas Red set long pass filter. Terminology and units used for cancellous and cortical bone histomorphometry are those recommended by the Histomorphometry Nomenclature Committee of the American Society for Bone and Mineral Research (53, 54).

Culture of BMMs and osteoclast formation

To obtain BMMs, the marrow was removed by flushing with a 26-gauge needle, and erythrocytes were lysed in 150 mM NH_4Cl, 10 mM $KHCO_3$, and 0.1 mM EDTA (pH 7.4). Cells were centrifuged, and the sediment was suspended in α-minimum essential medium (α-MEM) in the presence of 10% fetal bovine serum (FBS; both from Thermo Fisher Scientific, Waltham, MA) and recombinant human M-CSF at 30 ng/ml. M-CSF cDNA and expression vector were obtained from D. Fremont (St. Louis, MO), and M-CSF was purified as reported previously (55). Cells were seeded at a density of 300,000 cells/cm² and cultured for 3–4 days. Inversion of the *COIN* module was documented by PCR of genomic DNA using primers specific for the $Notch2^{\Delta PEST}$ allele (Table 7). For osteoclast formation, cells were collected following treatment with 0.05% trypsin/EDTA for 5 min and seeded at a density of 47,000 cells/cm² in α-MEM

Table 8
Primers used for qRT-PCR determinations
GenBank™ accession numbers identify the transcripts recognized by primer pairs.

Gene	Strand	Sequence 5′–3′	GenBank™ accession no.
Hes1	Forward Reverse	ACCAAAGACGGCCTCTGAGCACAGAAAGT ATTCTTGCCCTTCGCCTCTT	NM_008235
Hey1	Forward Reverse	ATCTCAACAACTACGCATCCCAGC GTGTGGGTGATGTCCGAAGG	NM_010423
Hey2	Forward Reverse	AGCGAGAACAATTACCCTGGGCAC GGTAGTTGTCGGTGAATTGGACCT	NM_013904
HeyL	Forward Reverse	CAGTAGCCTTTCTGAATTGCGAC AGCTTGGAGGAGCCCTGTTTC	NM_013905
Notch2^{WT}	Forward Reverse	CCATTGTGCCAACCTATCAT TTGAGGAGGCGTAACTGT	NM_010928[a]
Notch2$^{\Delta PEST}$	Forward Reverse	GGCTTTCCCACCTACCAT TAGTCGGGCACGTCGTAG	Not applicable
Rpl38	Forward Reverse	AGAACAAGGATAATGTGAAGTTCAAGGTTC CTGCTTCAGCTTCTCTGCCTTT	NM_001048057; NM_001048058; NM_023372
Tnfsf11	Forward Reverse	TATAGAATCCTGAGACTCCATGAAAAC CCCTGAAAGGCTTGTTTCATCC	NM_011613

[a] This recognizes a fragment coding for the PEST domain of Notch2.

with 10% FBS, M-CSF at 30 ng/ml, and recombinant murine Rankl at 10 ng/ml. Rankl cDNA and expression vector were obtained from M. Glogauer (Toronto, Canada), and GST-tagged Rankl was expressed and purified as described (56). Cultures were carried out until formation of multinucleated tartrate-resistant acid phosphatase (Trap)-positive cells. Trap enzyme histochemistry was conducted using a commercial kit (Sigma), in accordance with manufacturer's instructions. Trap-positive cells containing more than three nuclei were considered osteoclasts.

Osteoblast-enriched cell cultures

The parietal bones of 3–5-day-old *Notch2$^{COIN/COIN}$* mice were exposed to 1.2 units/ml Liberase™ TL (Sigma) for 20 min at 37 °C, and cells were extracted in five consecutive reactions (57). Cells from the last three digestions were pooled and seeded at a density of 10,000 cells/cm^2, as described (40). Osteoblast-enriched cells were cultured in Dulbecco's modified Eagle's medium (DMEM) supplemented with non-essential amino acids (both from Thermo Fisher Scientific), 20 mM HEPES, 100 μg/ml ascorbic acid (both from Sigma), and 10% heat-inactivated FBS (Atlanta Biologicals, Norcross, GA) in a humidified 5% CO_2 incubator at 37 °C. To induce inversion of the *COIN* allele, cells were infected with Ad-CMV-Cre, and parallel cultures infected with Ad-CMV-GFP (both from Vector Biolabs, Philadelphia, PA) served as controls (58). To this end, sub-confluent osteoblast-enriched cells were transferred to culture medium containing 2% heat-inactivated FBS for 1 h and exposed overnight to 100 multiplicity of infection of replication-defective recombinant adenoviruses. Cells were allowed to recover for 24 h in DMEM containing 10% heat-inactivated FBS and then seeded at a density of 22,000 cells/cm^2. Confluent cultures were exposed to medium supplemented with 5 mM β-glycerophosphate (Sigma) to induce osteoblast maturation. To document inversion of the *COIN* module, the presence of the *Notch2$^{\Delta PEST}$* allele was determined by PCR in genomic DNA using specific primers (Table 7).

RNA integrity and qRT-PCR

Total RNA was extracted from osteoblast-enriched cells with the RNeasy kit (Qiagen, Valencia, CA) and from homogenized bones with the micro RNeasy kit (Qiagen), in accordance with manufacturer's instructions. The integrity of the RNA was assessed by microfluidic electrophoresis on an Experion system (Bio-Rad), and only RNA with a quality indicator number equal to or higher than 7.0 was used for subsequent analysis (59, 60). Equal amounts of RNA were reverse-transcribed using the iScript RT-PCR kit (Bio-Rad) and amplified in the presence of specific primers (all primers from IDT; Table 8) with the iQ SYBR Green Supermix (Bio-Rad) at 60 °C for 35 cycles. Transcript copy number was estimated by comparison with a serial dilution of cDNA for *Hes1* (from American Type Culture Collection, ATCC; Manassas, VA), *Hey1* or *Hey2* (T. Iso, Los Angeles, CA), *HeyL* (D. Srivastava, Dallas, TX), or *Tnfsf11* (Source BioScience, Nottingham, UK) (61–64).

To monitor for the efficiency of the COIN inversion, primers designed to amplify a sequence of the *Notch2* transcript coding for the PEST domain were used (Table 8). These primers allow detection by qRT-PCR of the transcripts for *Notch2^{WT}* and *Notch2^{COIN}* but not for *Notch2$^{\Delta PEST}$*, because the latter lacks the sequences coding for the PEST domain. *Notch2^{WT}* and *Notch2^{COIN}* copy numbers were measured by comparing with a serial dilution of *Notch2* cDNA (Thermo Fisher Scientific). *Notch2$^{\Delta PEST}$* transcripts were detected with primers that generate an amplicon straddling the artificial splice junction generated within exon 34 of the targeted *Notch2* locus upon inversion of the *COIN* module (Table 8). Primers are specific for the *Notch2$^{\Delta PEST}$* mRNA and do not recognize the wild-type *Notch2* transcript or the *Notch2^{COIN}* mRNA prior to the *COIN* inversion. *Notch2$^{\Delta PEST}$* copy number was estimated by comparison with a serial dilution of an ~200 bp synthetic DNA template (IDT) cloned into pcDNA3.1(−) (Thermo Fisher Scientific) by isothermal single reaction assembly using commercially available reagents (New England Biolabs, Ipswich, MA) (65).

Amplification reactions were conducted in CFX96 qRT-PCR detection systems (Bio-Rad), and fluorescence was monitored during every PCR cycle at the annealing step. Data are expressed as copy number corrected for *Rpl38* expression estimated by comparison with a serial dilution of *Rpl38* (ATCC) (66).

Statistics

Data are expressed as means ± S.D. Statistical differences were determined by Student's *t* test or two-way analysis of variance with Holm-Šídák post hoc analysis for pairwise or multiple comparisons, respectively.

References

1. Fortini, M. E. (2009) Notch signaling: the core pathway and its posttranslational regulation. *Dev. Cell* **16,** 633–647
2. Kopan, R., and Ilagan, M. X. (2009) The canonical Notch signaling pathway: unfolding the activation mechanism. *Cell* **137,** 216–233
3. Kovall, R. A. (2007) Structures of CSL, notch and mastermind proteins: piecing together an active transcription complex. *Curr. Opin. Struct. Biol.* **17,** 117–127
4. Iso, T., Kedes, L., and Hamamori, Y. (2003) HES and HERP families: multiple effectors of the Notch signaling pathway. *J. Cell. Physiol.* **194,** 237–255
5. Groot, A. J., Habets, R., Yahyanejad, S., Hodin, C. M., Reiss, K., Saftig, P., Theys, J., and Vooijs, M. (2014) Regulated proteolysis of NOTCH2 and NOTCH3 receptors by ADAM10 and presenilins. *Mol. Cell. Biol.* **34,** 2822–2832
6. Baeten, J. T., and Lilly, B. (2015) Differential regulation of NOTCH2 and NOTCH3 contribute to their unique functions in vascular smooth muscle cells. *J. Biol. Chem.* **290,** 16226–16237
7. Liu, Z., Brunskill, E., Varnum-Finney, B., Zhang, C., Zhang, A., Jay, P. Y., Bernstein, I., Morimoto, M., and Kopan, R. (2015) The intracellular domains of Notch1 and Notch2 are functionally equivalent during development and carcinogenesis. *Development* **142,** 2452–2463
8. Yuan, Z., Friedmann, D. R., VanderWielen, B. D., Collins, K. J., and Kovall, R. A. (2012) Characterization of CSL (CBF-1, Su(H), Lag-1) mutants reveals differences in signaling mediated by Notch1 and Notch2. *J. Biol. Chem.* **287,** 34904–34916
9. Canalis, E., Giustina, A., and Bilezikian, J. P. (2007) Mechanisms of anabolic therapies for osteoporosis. *N. Engl. J. Med.* **357,** 905–916
10. Teitelbaum, S. L. (2007) Osteoclasts: what do they do and how do they do it? *Am. J. Pathol.* **170,** 427–435
11. Bianco, P., and Gehron Robey, P. (2000) Marrow stromal stem cells. *J. Clin. Invest.* **105,** 1663–1668
12. Zanotti, S., and Canalis, E. (2016) Notch signaling and the skeleton. *Endocr. Rev.* **37,** 223–253
13. Bai, S., Kopan, R., Zou, W., Hilton, M. J., Ong, C. T., Long, F., Ross, F. P., and Teitelbaum, S. L. (2008) NOTCH1 regulates osteoclastogenesis directly in osteoclast precursors and indirectly via osteoblast lineage cells. *J. Biol. Chem.* **283,** 6509–6518
14. Canalis, E., Adams, D. J., Boskey, A., Parker, K., Kranz, L., and Zanotti, S. (2013) Notch signaling in osteocytes differentially regulates cancellous and cortical bone remodeling. *J. Biol. Chem.* **288,** 25614–25625
15. Canalis, E., Parker, K., Feng, J. Q., and Zanotti, S. (2013) Osteoblast lineage-specific effects of Notch activation in the skeleton. *Endocrinology* **154,** 623–634
16. Engin, F., Yao, Z., Yang, T., Zhou, G., Bertin, T., Jiang, M. M., Chen, Y., Wang, L., Zheng, H., Sutton, R. E., Boyce, B. F., and Lee, B. (2008) Dimorphic effects of Notch signaling in bone homeostasis. *Nat. Med.* **14,** 299–305
17. Fukushima, H., Nakao, A., Okamoto, F., Shin, M., Kajiya, H., Sakano, S., Bigas, A., Jimi, E., and Okabe, K. (2008) The association of Notch2 and NF-κB accelerates RANKL-induced osteoclastogenesis. *Mol. Cell. Biol.* **28,** 6402–6412
18. Yorgan, T., Vollersen, N., Riedel, C., Jeschke, A., Peters, S., Busse, B., Amling, M., and Schinke, T. (2016) Osteoblast-specific Notch2 inactivation causes increased trabecular bone mass at specific sites of the appendicular skeleton. *Bone* **87,** 136–146
19. Zanotti, S., Smerdel-Ramoya, A., Stadmeyer, L., Durant, D., Radtke, F., and Canalis, E. (2008) Notch inhibits osteoblast differentiation and causes osteopenia. *Endocrinology* **149,** 3890–3899
20. Cheney, W. D. (1965) Acro-osteolysis. *Am. J. Roentgenol. Radium. Ther. Nucl. Med.* **94,** 595–607
21. Hajdu, N., and Kauntze, R. (1948) Cranio-skeletal dysplasia. *Br. J. Radiol.* **21,** 42–48
22. Gray, M. J., Kim, C. A., Bertola, D. R., Arantes, P. R., Stewart, H., Simpson, M. A., Irving, M. D., and Robertson, S. P. (2012) Serpentine fibula polycystic kidney syndrome is part of the phenotypic spectrum of Hajdu-Cheney syndrome. *Eur. J. Hum. Genet.* **20,** 122–124
23. Isidor, B., Lindenbaum, P., Pichon, O., Bézieau, S., Dina, C., Jacquemont, S., Martin-Coignard, D., Thauvin-Robinet, C., Le Merrer, M., Mandel, J. L., David, A., Faivre, L., Cormier-Daire, V., Redon, R., and Le Caignec, C. (2011) Truncating mutations in the last exon of NOTCH2 cause a rare skeletal disorder with osteoporosis. *Nat. Genet.* **43,** 306–308
24. Majewski, J., Schwartzentruber, J. A., Caqueret, A., Patry, L., Marcadier, J., Fryns, J. P., Boycott, K. M., Ste-Marie, L. G., McKiernan, F. E., Marik, I., Van Esch, H., FORGE Canada Consortium, Michaud, J. L., and Samuels, M. E. (2011) Mutations in NOTCH2 in families with Hajdu-Cheney syndrome. *Hum. Mutat.* **32,** 1114–1117
25. Simpson, M. A., Irving, M. D., Asilmaz, E., Gray, M. J., Dafou, D., Elmslie, F. V., Mansour, S., Holder, S. E., Brain, C. E., Burton, B. K., Kim, K. H., Pauli, R. M., Aftimos, S., Stewart, H., Kim, C. A., *et al.* (2011) Mutations in NOTCH2 cause Hajdu-Cheney syndrome, a disorder of severe and progressive bone loss. *Nat. Genet.* **43,** 303–305
26. Zhao, W., Petit, E., Gafni, R. I., Collins, M. T., Robey, P. G., Seton, M., Miller, K. K., and Mannstadt, M. (2013) Mutations in NOTCH2 in patients with Hajdu-Cheney syndrome. *Osteoporos. Int.* **24,** 2275–2281
27. Canalis, E., Schilling, L., Yee, S. P., Lee, S. K., and Zanotti, S. (2016) Hajdu Cheney mouse mutants exhibit osteopenia, increased osteoclastogenesis and bone resorption. *J. Biol. Chem.* **291,** 1538–1551
28. Economides, A. N., Frendewey, D., Yang, P., Dominguez, M. G., Dore, A. T., Lobov, I. B., Persaud, T., Rojas, J., McClain, J., Lengyel, P., Droguett, G., Chernomorsky, R., Stevens, S., Auerbach, W., Dechiara, T. M., *et al.* (2013) Conditionals by inversion provide a universal method for the generation of conditional alleles. *Proc. Natl. Acad. Sci. U.S.A.* **110,** E3179–E3188
29. Yang, M., Trettel, L. B., Adams, D. J., Harrison, J. R., Canalis, E., and Kream, B. E. (2010) Col3.6-HSD2 transgenic mice: A glucocorticoid loss-of-function model spanning early and late osteoblast differentiation. *Bone* **47,** 573–582
30. Adra, C. N., Boer, P. H., and McBurney, M. W. (1987) Cloning and expression of the mouse pgk-1 gene and the nucleotide sequence of its promoter. *Gene* **60,** 65–74
31. Beck, E., Ludwig, G., Auerswald, E. A., Reiss, B., and Schaller, H. (1982) Nucleotide sequence and exact localization of the neomycin phosphotransferase gene from transposon Tn5. *Gene* **19,** 327–336
32. Yoshikawa, Y., Kode, A., Xu, L., Mosialou, I., Silva, B. C., Ferron, M., Clemens, T. L., Economides, A. N., and Kousteni, S. (2011) Genetic evi-

dence points to an osteocalcin-independent influence of osteoblasts on energy metabolism. *J. Bone Miner. Res.* **26,** 2012–2025

33. Canalis, E., and Zanotti, S. (2016) Hajdu-Cheney syndrome, a disease associated with NOTCH2 mutations. *Curr. Osteoporos. Rep.* **14,** 126–131

34. Canalis, E., Sanjay, A., Yu, J., and Zanotti, S. (2017) An antibody of Notch2 reverses the osteopenic phenotype of Hajdu Cheney mutant male mice. *Endocrinology* **158,** 730–742

35. Adami, G., Rossini, M., Gatti, D., Orsolini, G., Idolazzi, L., Viapiana, O., Scarpa, A., and Canalis, E. (2016) Hajdu Cheney syndrome; report of a novel NOTCH2 mutation and treatment with denosumab. *Bone* **92,** 150–156

36. Hilton, M. J., Tu, X., Wu, X., Bai, S., Zhao, H., Kobayashi, T., Kronenberg, H. M., Teitelbaum, S. L., Ross, F. P., Kopan, R., and Long, F. (2008) Notch signaling maintains bone marrow mesenchymal progenitors by suppressing osteoblast differentiation. *Nat. Med.* **14,** 306–314

37. Zanotti, S., and Canalis, E. (2014) Notch1 and Notch2 expression in osteoblast precursors regulates femoral microarchitecture. *Bone* **62,** 22–28

38. Dong, Y., Jesse, A. M., Kohn, A., Gunnell, L. M., Honjo, T., Zuscik, M. J., O'Keefe, R. J., and Hilton, M. J. (2010) RBPjκ-dependent Notch signaling regulates mesenchymal progenitor cell proliferation and differentiation during skeletal development. *Development* **137,** 1461–1471

39. Mead, T. J., and Yutzey, K. E. (2009) Notch pathway regulation of chondrocyte differentiation and proliferation during appendicular and axial skeleton development. *Proc. Natl. Acad. Sci. U.S.A.* **106,** 14420–14425

40. Canalis, E., Zanotti, S., and Smerdel-Ramoya, A. (2014) Connective tissue growth factor is a target of Notch signaling in cells of the osteoblastic lineage. *Bone* **64,** 273–280

41. Glatt, V., Canalis, E., Stadmeyer, L., and Bouxsein, M. L. (2007) Age-related changes in trabecular architecture differ in female and male C57BL/6J mice. *J. Bone Miner. Res.* **22,** 1197–1207

42. Zhang, M., Xuan, S., Bouxsein, M. L., von Stechow, D., Akeno, N., Faugere, M. C., Malluche, H., Zhao, G., Rosen, C. J., Efstratiadis, A., and Clemens, T. L. (2002) Osteoblast-specific knockout of the insulin-like growth factor (IGF) receptor gene reveals an essential role of IGF signaling in bone matrix mineralization. *J. Biol. Chem.* **277,** 44005–44012

43. Salie, R., Kneissel, M., Vukevic, M., Zamurovic, N., Kramer, I., Evans, G., Gerwin, N., Mueller, M., Kinzel, B., and Susa, M. (2010) HEY1 regulates bone mass and cartilage hypertrophy by linking BMP signaling with the PTH receptor. *Bone* **46,** 680–694

44. Tu, X., Chen, J., Lim, J., Karner, C. M., Lee, S. Y., Heisig, J., Wiese, C., Surendran, K., Kopan, R., Gessler, M., and Long, F. (2012) Physiological notch signaling maintains bone homeostasis via RBPjk and Hey upstream of NFATc1. *PLoS Genet.* **8,** e1002577

45. Zanotti, S., and Canalis, E. (2013) Hairy and enhancer of split-related with YRPW Motif (HEY)2 regulates bone remodeling in mice. *J. Biol. Chem.* **288,** 21547–21557

46. Canalis, E., and Zanotti, S. (2017) Hairy and enhancer of split-related with YRPW Motif-like (HeyL) is dispensable for bone remodeling in mice. *J. Cell. Biochem.* **118,** 1819–1826

47. Buchholz, F., Angrand, P. O., and Stewart, A. F. (1996) A simple assay to determine the functionality of Cre or FLP recombination targets in genomic manipulation constructs. *Nucleic Acids Res.* **24,** 3118–3119

48. Buchholz, F., Angrand, P. O., and Stewart, A. F. (1998) Improved properties of FLP recombinase evolved by cycling mutagenesis. *Nat. Biotechnol.* **16,** 657–662

49. Tang, S. H., Silva, F. J., Tsark, W. M., and Mann, J. R. (2002) A Cre/loxP-deleter transgenic line in mouse strain 129S1/SvImJ. *Genesis* **32,** 199–202

50. Clausen, B. E., Burkhardt, C., Reith, W., Renkawitz, R., and Förster, I. (1999) Conditional gene targeting in macrophages and granulocytes using LysMcre mice. *Transgenic Res.* **8,** 265–277

51. Takeda, K., Clausen, B. E., Kaisho, T., Tsujimura, T., Terada, N., Förster, I., and Akira, S. (1999) Enhanced Th1 activity and development of chronic enterocolitis in mice devoid of Stat3 in macrophages and neutrophils. *Immunity* **10,** 39–49

52. Bouxsein, M. L., Boyd, S. K., Christiansen, B. A., Guldberg, R. E., Jepsen, K. J., and Müller, R. (2010) Guidelines for assessment of bone microstructure in rodents using micro-computed tomography. *J. Bone Miner. Res.* **25,** 1468–1486

53. Dempster, D. W., Compston, J. E., Drezner, M. K., Glorieux, F. H., Kanis, J. A., Malluche, H., Meunier, P. J., Ott, S. M., Recker, R. R., and Parfitt, A. M. (2013) Standardized nomenclature, symbols, and units for bone histomorphometry: a 2012 update of the report of the ASBMR Histomorphometry Nomenclature Committee. *J. Bone Miner. Res.* **28,** 2–17

54. Parfitt, A. M., Drezner, M. K., Glorieux, F. H., Kanis, J. A., Malluche, H., Meunier, P. J., Ott, S. M., and Recker, R. R. (1987) Bone histomorphometry: standardization of nomenclature, symbols, and units. Report of the ASBMR Histomorphometry Nomenclature Committee. *J. Bone Miner. Res.* **2,** 595–610

55. Lee, S. H., Rho, J., Jeong, D., Sul, J. Y., Kim, T., Kim, N., Kang, J. S., Miyamoto, T., Suda, T., Lee, S. K., Pignolo, R. J., Koczon-Jaremko, B., Lorenzo, J., and Choi, Y. (2006) v-ATPase V0 subunit d2-deficient mice exhibit impaired osteoclast fusion and increased bone formation. *Nat. Med.* **12,** 1403–1409

56. Wang, Y., Lebowitz, D., Sun, C., Thang, H., Grynpas, M. D., and Glogauer, M. (2008) Identifying the relative contributions of Rac1 and Rac2 to osteoclastogenesis. *J. Bone Miner. Res.* **23,** 260–270

57. Yesil, P., Michel, M., Chwalek, K., Pedack, S., Jany, C., Ludwig, B., Bornstein, S. R., and Lammert, E. (2009) A new collagenase blend increases the number of islets isolated from mouse pancreas. *Islets* **1,** 185–190

58. Zanotti, S., Smerdel-Ramoya, A., and Canalis, E. (2013) Nuclear factor of activated T-cells (Nfat)c2 inhibits Notch signaling in osteoblasts. *J. Biol. Chem.* **288,** 624–632

59. Nazarenko, I., Lowe, B., Darfler, M., Ikonomi, P., Schuster, D., and Rashtchian, A. (2002) Multiplex quantitative PCR using self-quenched primers labeled with a single fluorophore. *Nucleic Acids Res.* **30,** e37

60. Nazarenko, I., Pires, R., Lowe, B., Obaidy, M., and Rashtchian, A. (2002) Effect of primary and secondary structure of oligodeoxyribonucleotides on the fluorescent properties of conjugated dyes. *Nucleic Acids Res.* **30,** 2089–2195

61. Glinka, A., Wu, W., Delius, H., Monaghan, A. P., Blumenstock, C., and Niehrs, C. (1998) Dickkopf-1 is a member of a new family of secreted proteins and functions in head induction. *Nature* **391,** 357–362

62. Iso, T., Sartorelli, V., Chung, G., Shichinohe, T., Kedes, L., and Hamamori, Y. (2001) HERP, a new primary target of Notch regulated by ligand binding. *Mol. Cell. Biol.* **21,** 6071–6079

63. Lian, J., Stewart, C., Puchacz, E., Mackowiak, S., Shalhoub, V., Collart, D., Zambetti, G., and Stein, G. (1989) Structure of the rat osteocalcin gene and regulation of vitamin D-dependent expression. *Proc. Natl. Acad. Sci. U.S.A.* **86,** 1143–1147

64. Nakagawa, O., Nakagawa, M., Richardson, J. A., Olson, E. N., and Srivastava, D. (1999) HRT1, HRT2, and HRT3: a new subclass of bHLH transcription factors marking specific cardiac, somitic, and pharyngeal arch segments. *Dev. Biol.* **216,** 72–84

65. Gibson, D. G., Young, L., Chuang, R. Y., Venter, J. C., Hutchison, C. A., 3rd., and Smith, H. O. (2009) Enzymatic assembly of DNA molecules up to several hundred kilobases. *Nat. Methods* **6,** 343–345

66. Kouadjo, K. E., Nishida, Y., Cadrin-Girard, J. F., Yoshioka, M., and St-Amand, J. (2007) Housekeeping and tissue-specific genes in mouse tissues. *BMC. Genomics* **8,** 127

ASBMB